

Machine learning assisted history matching for a deepwater lobe system

Honggeun Jo ^{a,*}, Wen Pan ^a, Javier E. Santos ^a, Hyungsik Jung ^b, Michael J. Pyrcz ^{a,c,d}

^a Hildebrand Department of Petroleum and Geosystems Engineering, The University of Texas at Austin, Texas, USA

^b AI Vision Lab., Samsung SDS, Seoul, South Korea

^c Bureau of Economic Geology, Jackson School of Geosciences, The University of Texas at Austin, Texas, USA

^d Jackson School of Geosciences, The University of Texas at Austin, Texas, USA



ARTICLE INFO

Keywords:

Rule-based model
Generative adversarial network
Machine learning
Ensemble-based modeling
History matching
Ensemble kalman filter

ABSTRACT

High exploration costs resulting in sparse datasets and complicated geological structures in deepwater depositional systems make the reservoir characterization extremely difficult. To meet this challenge, rule-based geostatistical subsurface modeling has been developed to fill this data gap with enhanced integration of geological concepts for deepwater reservoirs based on geological rules constrained by this sparse well data. The rule-based model simulates sediment dynamics through depositional rules to calculate reservoir architecture and the associated rock properties distributions. As a result, rule-based models incorporate conceptual and qualitative information, such as temporal deposition sequence and consequent compensational stacking patterns. Integrating quantitative data, such as fluid production history, is a remaining obstacle to the broad application of rule-based subsurface models.

We propose a new machine learning assisted history matching workflow for rule-based models. First, multiple rule-based models are calculated as training data for a Generative Adversarial Network (GAN). The successfully trained GAN enables exploration of the latent reservoir manifold with only a small number of numeric values (i.e., latent random vector); this is a massive reduction in the dimensionality of potential subsurface models. The initial ensemble models, generated by the trained GAN with a range of latent random vectors, are coupled with physics-based reservoir flow simulation to obtain production forecasts. Ensemble Kalman filter (EnKF) updates the latent random vectors of the ensemble by minimizing the misfit (i.e., error norm) between the production forecasts and the production observation over time.

Our proposed workflow finds an ensemble of optimized reservoir models that honor realistic geological heterogeneity and production history. Besides, as the GAN's latent random vectors are Gaussian distributed, one of the fundamental mathematical assumptions of EnKF, this workflow effectively alleviates possible artifacts (e.g., filter divergence or overshooting) in EnKF. Moreover, this proposed workflow is more computationally efficient than updating the entire high-dimensional reservoir properties and removes the limitation to only Gaussian simulation models with their limited geological realism. The proposed workflow may be expanded to various reservoir depositional settings.

1. Introduction

The complicated reservoir structure in deepwater and multi-billion-dollar exploration and development make it more important than ever to characterize these subsurface depositional systems accurately (McHargue et al., 2011). Due to the high cost and technical challenges of exploration, a limited number of available wells (well logs and limited cores) and low-resolution seismic may be the only data sources to investigate the subsurface. Even though seismic interpretation can detect the subsurface rock facies distribution and their associated

petrophysical properties, there are many significant sub-seismic resolution heterogeneities and geologic features that must be integrated for accurate predictions with reasonable uncertainty models. These heterogeneities and features cannot be fully resolved from seismic images (Sullivan et al., 2004; Deptuck et al., 2008; Bertoncello et al., 2013; Pyrcz et al., 2015; Cho et al., 2018; Cho, 2021); therefore, we rely on geostatistical realizations of the reservoir heterogeneity. Rule-based modeling has been an alternative approach to calculate geostatistical models and quantify the uncertainty with enhanced geological realism for deepwater subsurface systems by combining the geological rules

* Corresponding author.

E-mail address: honggeun.jo@utexas.edu (H. Jo).

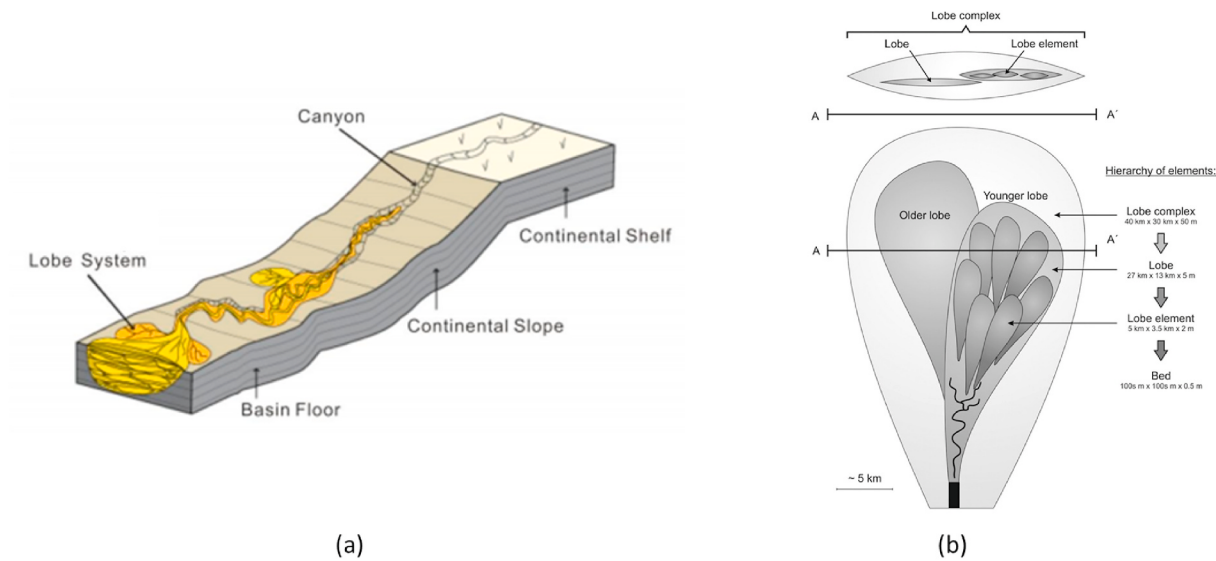


Fig. 1. Deepwater lobe system. (a) Block diagram of the lobe system (Bouma and Stone, 2000) and (b) associated hierarchical structure (Groenenberg et al., 2010). Note that sediment flows from the upper-right to lower-left in (a), whereas it flows from bottom to top (b).

- Center of top
- Center of bottom

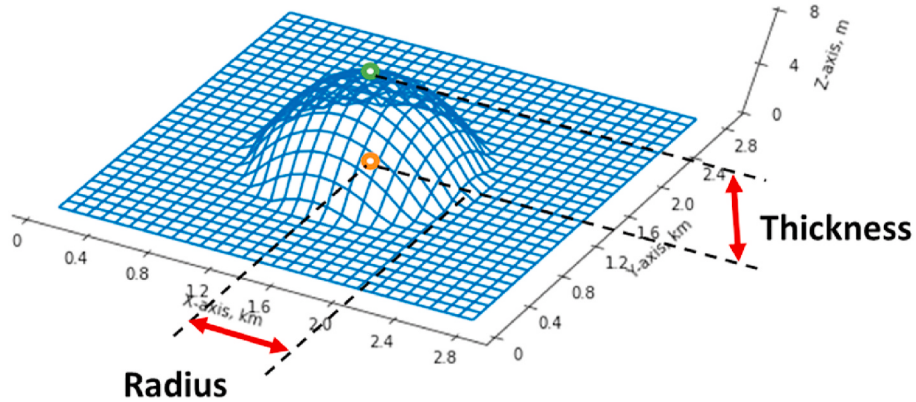


Fig. 2. Lobe element geometry. Paraboloid, isotropic lobe shape with a 750 m radius and 4 m thickness (modified from Xie et al. (2001)).

with the sparse well data (Pyrcz et al., 2005; Zhang et al., 2009; Michael et al., 2010). Improved realism is achieved by integrating qualitative information such as geological concepts, e.g., knowledge of depositional processes from experience-rich geologists (Michael et al., 2012; Pyrcz et al., 2015). These rules constrain the temporal sequence of deposit or consequent depositional pattern, yet conditioning the models to fluid production history remains as an important challenge.

To address the challenge of constraining subsurface models by fluid production history, various researchers have studied ensemble-based history matching (extensively summarized in Jung et al., 2018). Instead of a deterministic model, a group of subsurface models, known as an ensemble, is calibrated to match production history for accurate assessment of prediction uncertainty through physics-based forecasting with the resulting history matched ensemble of models. Evensen (1994) first suggested the ensemble Kalman filter (EnKF), which has a few advantages like an established mathematical theoretical pedigree and flexible application to multiple data types. After Nævdal et al. (2002) successfully applied EnKF to near-wellbore monitoring, EnKF has been

widely used for subsurface model history matching (Gu and Oliver, 2007; Oliver et al., 2011; Emerick and Reynolds, 2012; Jo et al., 2017). One of the obstacles in broadening applications of EnKF is the large dimensionality of the subsurface model features (e.g., porosity or permeability states often >10 million cells) coupled with computationally expensive reservoir simulation, which makes the EnKF history matching process extremely slow and at times impractical. Numerous methods for parameterization have developed to address the dimensionality challenge through the representation of the high-dimensional subsurface model with a projection to relatively low-dimensional parameter space, such as 1) principal component analysis (PCA) (Sarma et al., 2008; Vo and Durlofsky, 2016; Kang et al., 2020), 2) discrete cosine transform (DCT) (Jafarpour and McLaughlin, 2008; Kim et al., 2016; Jung et al., 2017), and 3) level set (Moreno and Aanonsen, 2007; Chang et al., 2019).

In addition to dimensionality reduction, GAN representation through random latent vectors converts the non-Gaussian prior subsurface model parameters to a vector of Gaussian parameters. Therefore, the

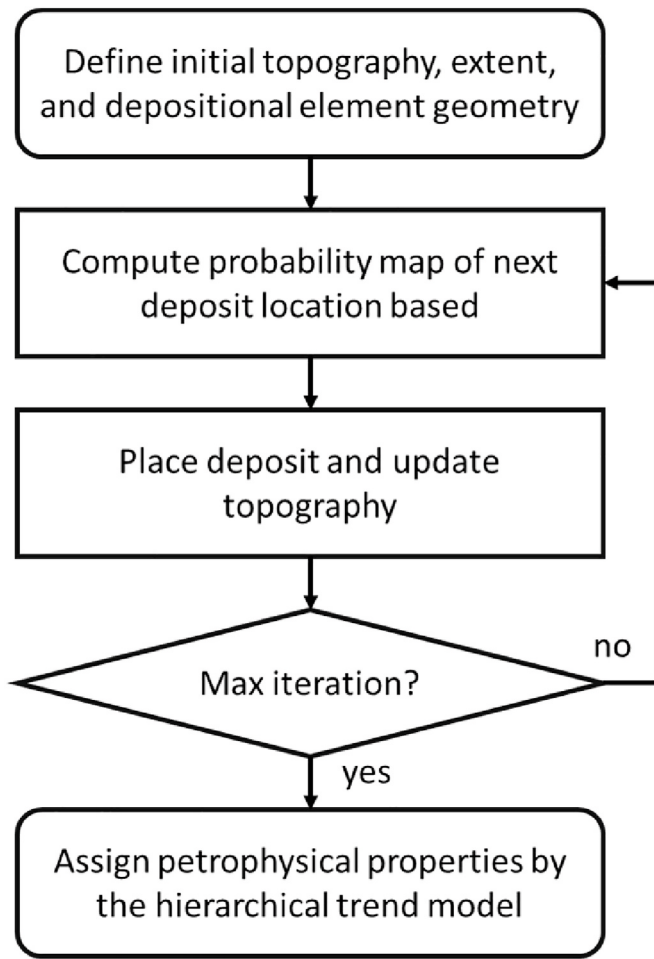


Fig. 3. The workflow of the rule-based model.

transformed parameters follow the underlying Gaussian assumption of EnKF (Jung et al., 2018). For example, the channelized geological model consists of more than two facies, so initial model variables (e.g., porosity or permeability) follow the multi-modal distribution. If a geomodeler applies EnKF to the original model variables, the updated subsurface model features tend to be Gaussian distributed; therefore, the conventional EnKF workflow is in general not able to conserve geological realism for the deepwater lobe geological setting.

Recent developments in deep learning algorithms improve subsurface spatial analysis, specifically geoscience and geostatistical subsurface modeling workflows (Mosser et al., 2017; Santos et al., 2020; Jo et al., 2020; Park et al., 2021; Santos et al., 2021). Generative adversarial network (GAN) is a novel technique for training a generative model, which generates new realizations that follow the intractable key geometric and statistical characteristics of the training dataset (Goodfellow et al., 2014). GAN has been investigated for parameterization, imputation, and generation of subsurface models with competitive results in capturing high-visual quality (Laloy et al., 2018; Chan and Elsheikh, 2019) as well as flexibility in coupling with other machine learning algorithms, such as semantic image inpainting for spatial data conditioning (Zhang et al., 2019; Jo et al., 2019). Moreover, recent work demonstrates that GANs effectively perform parameterizations in multi-point statistics subsurface model (Laloy et al., 2018; Zhang et al., 2019), complex microporous media (Mosser et al., 2017), and complicated subsurface heterogeneity (Jo et al., 2019; Canchumuni et al., 2020) with successful dimensionality reductions of several orders of magnitude.

We propose a novel machine learning assisted method to condition

subsurface models through ensemble-based history matching. We apply EnKF to update the subsurface models, not by direct calibration of petrophysical features (e.g., permeability) of individual grid cells, but by tuning the random latent vectors of a trained GAN. We demonstrated our proposed workflow on the deepwater lobe reservoir. Note that in the demonstration, porosity is assumed to be constant in the reservoir, and only permeability is updated through the workflow. Our proposed workflow is differentiated from previous subsurface data conditioning GAN-based workflows for conditioning subsurface models to static data (e.g., well-log or core) through either inference neural network (Chan and Elsheikh, 2019) or image inpainting algorithms (Jo et al., 2019; Zhang et al., 2019). Instead, this study focuses more on integrating dynamic data (e.g., fluid production history) to improve the accuracy in fluid production forecasts by combining an ensemble-based history matching algorithm.

To develop and demonstrate our proposed workflow, we include the following sections. In Section 2, we introduce methodological backgrounds, including rule-based model, EnKF, and GAN, as well as our proposed workflow, GAN-EnKF. In Section 3, we demonstrate our proposed method with the history matching for a deepwater lobe subsurface model. In Section 4, we conclude our work.

2. Methodology

The proposed workflow includes the following steps:

1. Calculate an ensemble of rule-based geostatistical models that integrate available geological concepts and span the range of geologic uncertainty
2. Train a GAN with the ensemble of rule-based models
3. Apply EnKF assimilation production data through the random vector of the trained GAN

In this section, we further cover prerequisites for each of these steps, including a discussion of the importance of rule-based models to reproduce realistic geological features for the deepwater depositional system (section 2.1.) along with the theoretical backgrounds of EnKF (section 2.2.) and GAN (section 2.3.). Then we introduce the details for our proposed method known as GAN-EnKF (section 2.4.).

2.1. Rule-based methods for modeling deepwater lobe systems

Rule-based geostatistical methods simulate sedimentary dynamics, sequential placement of depositional objects, to calculate subsurface heterogeneity models with the realistic spatial distributions of petrophysical properties (Pyrcz, 2004; Pyrcz et al., 2015; Jo et al., 2019). A few intuitive geological rules for the sequential deposition of sediments enable realistic reservoir heterogeneity, continuity, and spatial organization of petrophysical property distributions that are impractical to obtain using conventional geostatistical pixel- and object-based subsurface modeling methods. Rule-based models have two main advantages: 1) straightforward qualitative geology concept integration into subsurface models and 2) reproduction of a realistic connectivity model (Pyrcz and Deutsch, 2014; Pyrcz et al., 2015). Rule-based models integrate depositional element geometry (Xie et al., 2001; Pyrcz et al., 2005), lithofacies trends (Pyrcz and Deutsch, 2014), and the associated stacking pattern of depositional objects (Straub et al., 2009; Wang et al., 2011; Straub and Pyles, 2012). Moreover, Pyrcz et al. (2015) demonstrate that rule-based models generate realistic connectivity in subsurface models to improve fluid production forecasts, predictions with uncertainty. Various authors discuss rule-based model developments and applications for deepwater depositional systems (Xie et al., 2001; Pyrcz, 2004; Michael et al., 2010; Bertoncello et al., 2013) and fluvial depositional systems (Cojan et al., 2005; Pyrcz et al. 2009).

We demonstrate the proposed workflow for production data conditioning with a rule-based deepwater lobe depositional system model. For

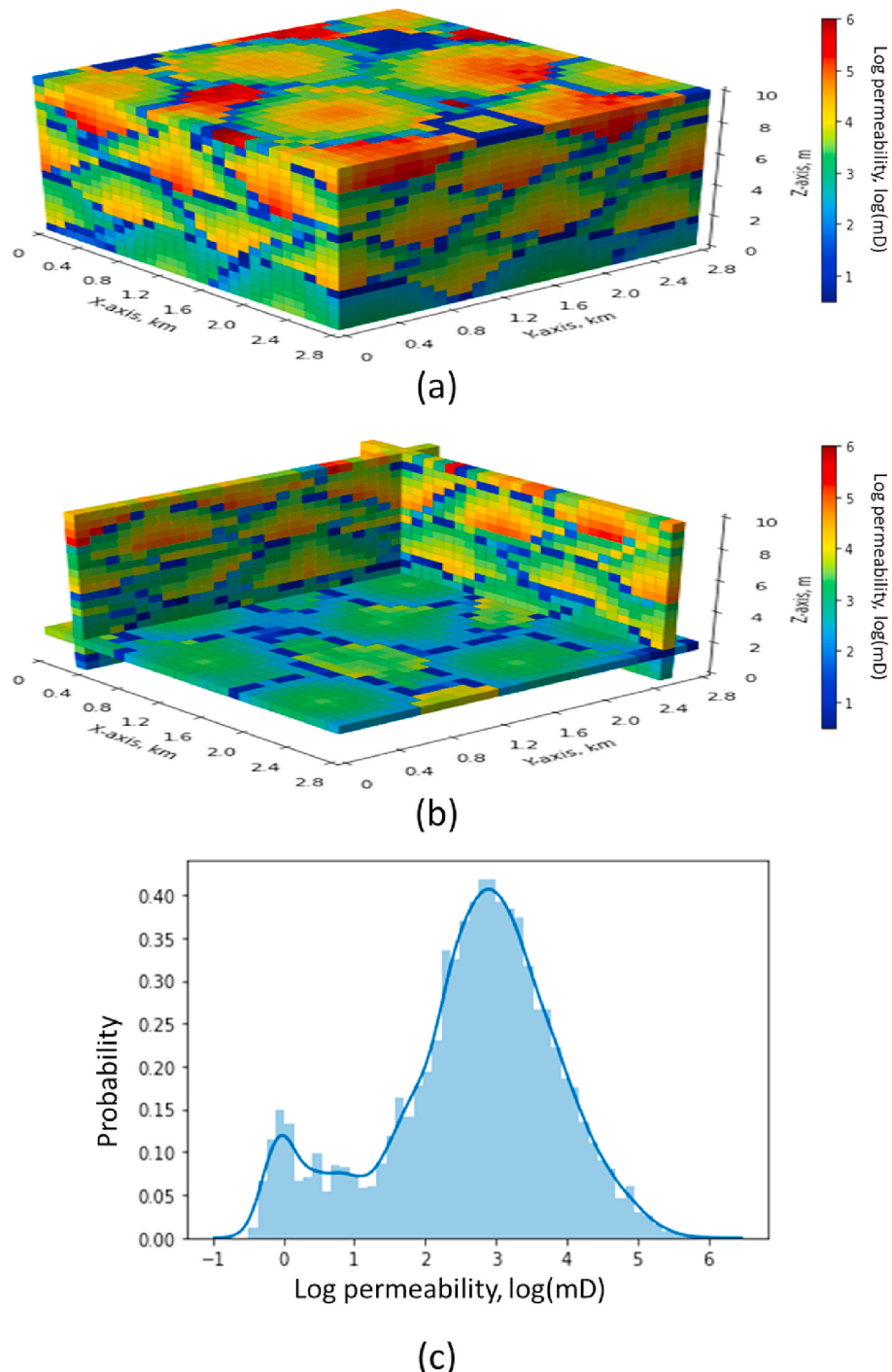


Fig. 4. Example of a rule-based model. (a) 3D permeability model, (b) fence diagram of the permeability model, and (c) distribution of permeability.

In this rule-based model, we use a hierarchical concept (i.e., a multiscale modeling framework) that subdivides deposits based on the distinct changes in depositional characteristics such as geometry, orientation, and trend. This follows the hierarchical architecture model with lobe complexes as the large-scale geometry comprises multiple lobe elements (Abreu et al., 2003; Sullivan et al., 2004; Deptuck et al., 2008; Prélat et al., 2009; Koo et al. 2016). Fig. 1 provides an illustrative block diagram for the deepwater lobe system and its hierarchical structure. The lobe geometry and associated stacking pattern have a significant impact on subsurface fluid flow due to the unique superposition of lobe margin (i.e., low permeability) and inner lobe (i.e., high permeability) in the consequent stacking pattern (Mutti and Normark 1987).

Three geological model parameters condition the rule-based model to fit a range of hierarchical structures that occur in natural systems. The first geological input is lobe element geometry. The typical aspect ratio of a lobe element (ratio of length to width) varies from one to three (Deptuck et al., 2008; Zhang et al. 2016). In this study, we assume isotropic lobe elements (with aspect ratio equal to one) to assess a generalized outcome by removing the effect of sediment flow direction. Fig. 2 shows the geometry of individual lobe geometry, similar to Xie et al. (2001). Given isotropic lobe elements, the lobe element geometric parameters are the horizontal radius and maximum thickness.

The second geological input is the compositional exponent to constrain the lobe elements' stacking pattern. In each iteration of the

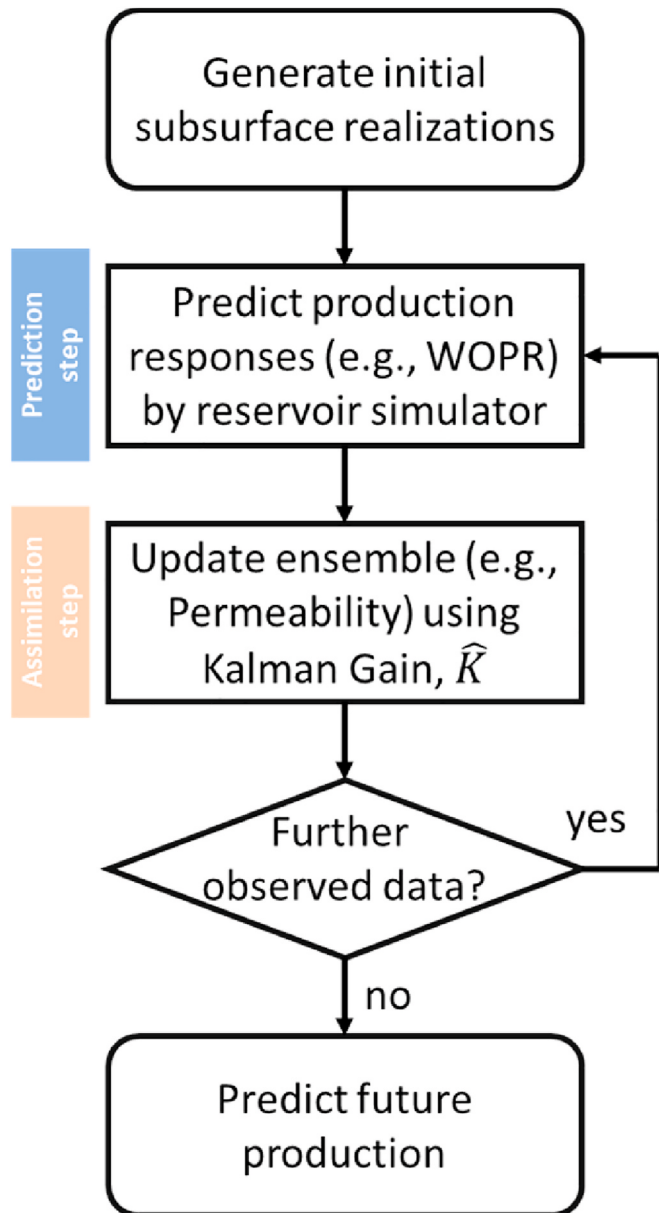


Fig. 5. The workflow of a standard EnKF.

sedimentary simulation, the next deposit's position is determined based on the probability map calculated as a function of the inverse of the minimax normalized compositional surface topography raised to an exponent. This compositional exponent determines the degree of compensational stacking, the tendency for sediments to preferentially deposit in topographic lows (Straub et al., 2009). Jo et al. (2019) demonstrate the effect of the compositional exponent in the rule-based model for the deepwater lobe system. The last geological model parameter constrains the hierarchical trend model of petrophysical properties over lobe elements within the lobe complexes (Pyracz, 2004; Pyracz et al., 2005).

The rule-based model starts with a predefined initial bathymetry, and one lobe element is deposited sequentially in each simulation iteration. Once a new lobe element is deposited on the current compositional surface, the topography is updated, resulting in an update to the probability map for the next lobe element location. Lobe elements are added until the subsurface model volume is filled. Rock properties (e.g., porosity and permeability) are assigned based on the hierarchical trend model, anchored to the individual lobe element surfaces (Pyracz et al.,

2005). For an example of a hierarchical trend, the inner lobe element has sandy rock, whereas the lobe's margin is covered by shaly rocks, and over the lobe complex scale, a coarsening-up trend exists due to system progradation. Fig. 3 shows the workflow of the rule-based model. For a set of training data to demonstrate our proposed method, we assume perfect compensation and lobe elements of 750 m radius and 4 m maximum thickness. See Fig. 4 for an example realization of this rule-based model. As the rule-based modeling method works in a grid-free framework (Pyracz et al., 2015), rule-based models enable preserving high-resolution transitions in horizontal and vertical directions, depending on the number of discretizing grid blocks. In this study, we discretize a rule-based model by 20 grid blocks in the z-direction, and each grid block has 0.5 m of thickness. Therefore, gradational changes in permeability within a lobe (i.e., 4 m maximum thickness) are observed in Fig. 4. If the number of grid blocks decreases, this transition between high-permeability rocks to low-permeability rocks will be neglected.

2.2. Ensemble Kalman filter (EnKF)

EnKF is an ensemble-based history matching method that assimilates available dynamic data into the subsurface models by minimizing the error covariance between static variables and dynamic responses among the multiple subsurface models (Katzfuss et al., 2016; Jung et al., 2018). With proper dynamic data assimilation, the subsurface models' estimates should follow the observed production history. Ensemble-based history matching represents each subsurface model (i.e., equiprobably realization, ensemble member) by a state vector that contains static variables and dynamic responses. The static variables, such as porosity and permeability, are time-independent during production in case of negligible compaction reservoir conditions. On the other hand, dynamic responses, e.g., production rate or bottom hole pressure, are time-dependent during production, and these dynamic responses are computed by running a reservoir simulator. Note that the true static variables are inaccessible, but the dynamic responses are production measurements from the real oil production field. For example, the permeability is updated to match historical fluid production over 500 days of operation. The state vector is represented by Equation (1):

$$\mathbf{y}_{k,i} = \begin{bmatrix} \mathbf{m}_{k,i}^s \\ \mathbf{d}_{k,i} \end{bmatrix} \quad (1)$$

where $\mathbf{y}_{k,i}$ is the state vector of the i^{th} ensemble member at the k^{th} time level. A state vector consists of static variables (m^s) and dynamic variables (d). To represent the entire ensemble, we concatenate the state vector to make the state matrix, as shown in Equation (2):

$$\mathbf{Y}_k = [\mathbf{y}_{k,1}, \mathbf{y}_{k,2}, \mathbf{y}_{k,3}, \dots, \mathbf{y}_{k,N_e}] = \begin{bmatrix} \mathbf{m}_{k,1}^s, \mathbf{m}_{k,2}^s, \mathbf{m}_{k,3}^s, \dots, \mathbf{m}_{k,N_e}^s \\ \mathbf{d}_{k,1}, \mathbf{d}_{k,2}, \mathbf{d}_{k,3}, \dots, \mathbf{d}_{k,N_e} \end{bmatrix} = \begin{bmatrix} \mathbf{M}_k^s \\ \mathbf{D}_k \end{bmatrix} \quad (2)$$

where N_e denotes the number of subsurface models that compose the ensemble. Moreover, M_k^s and D_k are concatenated static variables and dynamic responses of the ensemble. Note that the dimension of the state matrix is $(N_s + N_d) \times N_e$, where N_s and N_d are the number of static and dynamic variables, respectively.

EnKF consists of two main computational steps: prediction and assimilation. In the prediction step, reservoir simulation computes the dynamic response of the ensemble until the next observed data are available. The assimilation step updates the ensemble by comparing their predicted dynamic responses (from reservoir simulation) and the observed measurements through Equation (3). The change of the ensemble member is proportional to Kalman gain (\hat{K}) and the misfit between the observed measurements and the predicted dynamic responses. Kalman gain is computed by Equation (4) and is derived to minimize the estimated error covariance in Equation (5). A detailed derivation of Kalman gain is summarized in Katzfuss et al. (2016) and

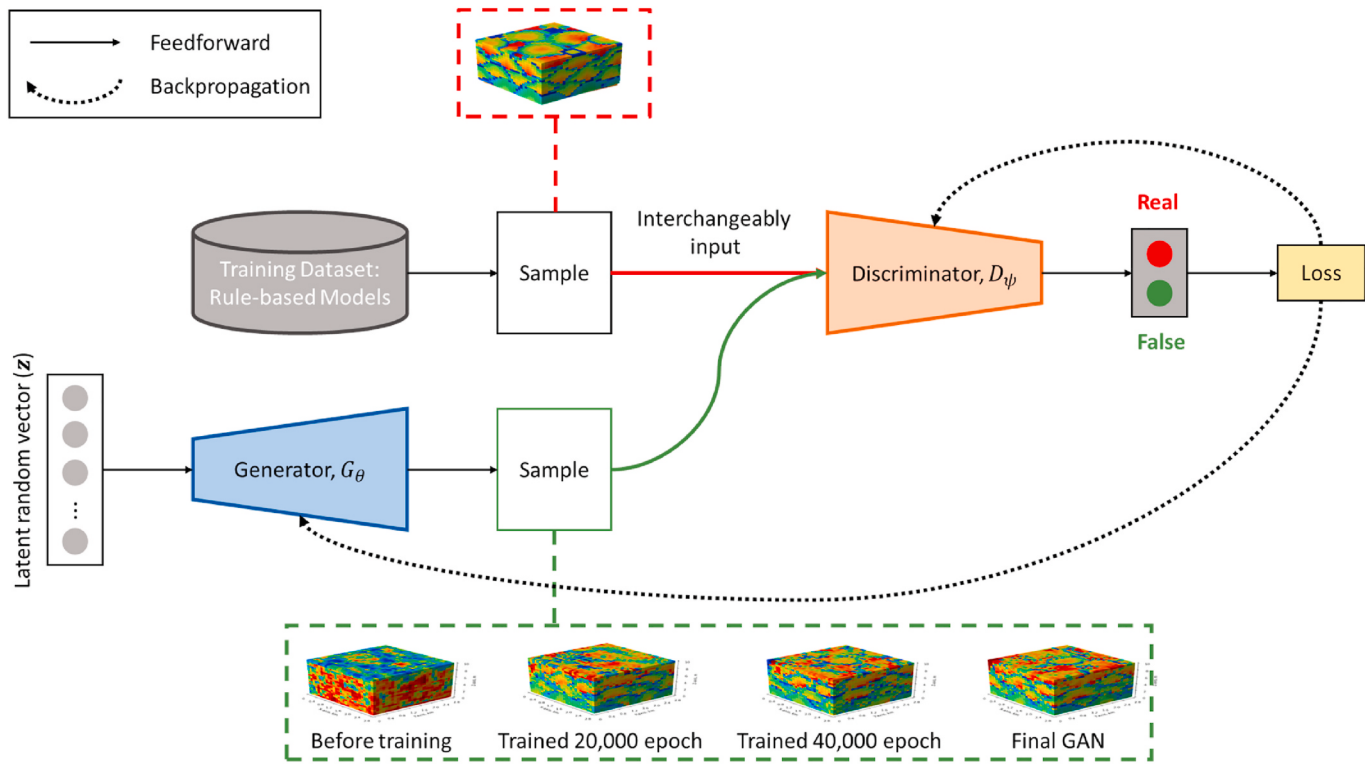


Fig. 6. Schematic diagram of GAN for the rule-based model (revised from Jo et al. (2020)). Red dashed box indicates an example of rule-based models and a green dashed box indicates $G_\theta(z)$, with a fixed z , at each training epoch. As the generator is trained, the realization becomes more and more realistic (e.g., hierarchical trend, stacking pattern of lobes, and depositional element geometry as innated in the rule-based model). The training iteration continues until there is no significant improvement in realizations comparing to the previous ones by ocular inspection. (For interpretation of the references to colour in this figure legend, the reader is referred to the Web version of this article.)

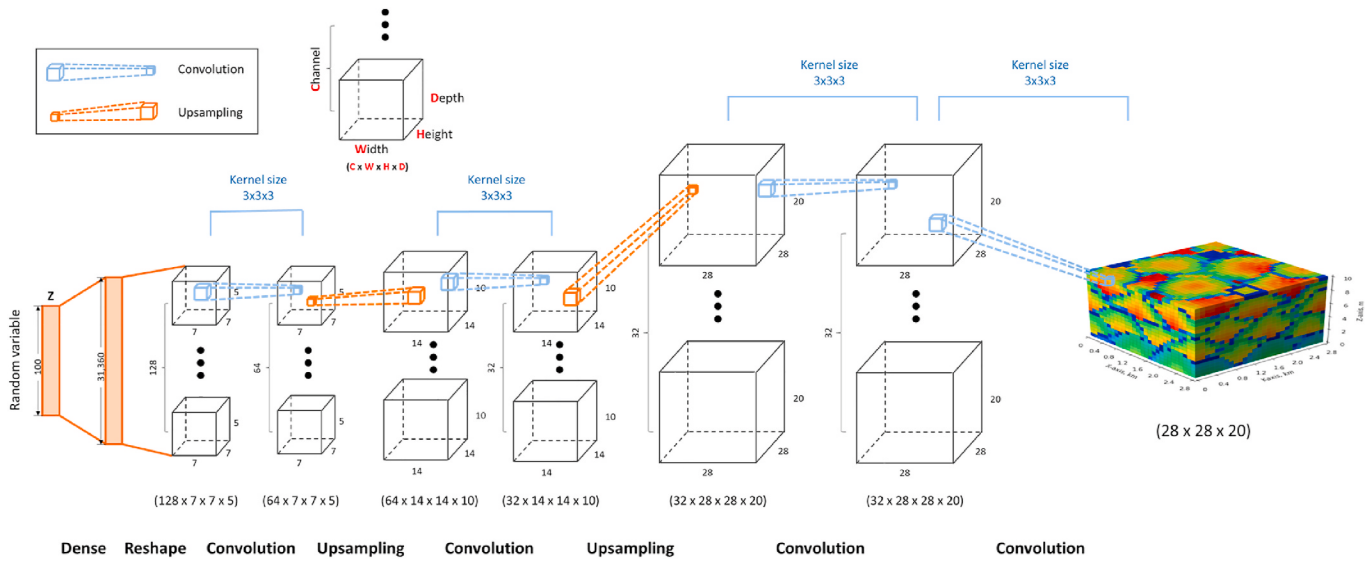


Fig. 7. Structure of the generator, $G_\theta(z)$. θ is involved in Dense and Convolution layers and the number of trainable parameters (i.e., θ) in generator is 3,892,641.

Jung et al. (2018). Prediction and assimilation steps are iteratively done until the end of the history matching process. Fig. 5 shows a typical EnKF workflow.

$$Y_k^a = Y_k^p + \hat{K}(D_{obs,k} - D_k) \quad (3)$$

$$\hat{K} = C_y^p H^T (H C_y^p H^T + C_D)^{-1} \quad (4)$$

$$C_y^p = \frac{1}{N_e - 1} (Y_k^p - \bar{Y}_k^p) (Y_k^p - \bar{Y}_k^p)^T = \begin{bmatrix} Cov(m_k^s, m_k^s) & Cov(m_k^s, d_k) \\ Cov(d_k, m_k^s) & Cov(d_k, d_k) \end{bmatrix} \quad (5)$$

where superscripts a and p denote post-assimilated and pre-assimilated, respectively. $D_{obs,k}$ and D_k are the observed measurement and the predicted dynamic response of ensemble at the k^{th} time level. Moreover, C_D represents the measurement error covariance matrix and contains the

Table 1

Structure of generator with associated activate function and hyperparameters.

Layer	Type	Output dimension (channel, width, height, depth)	Kernel size	Stride	Activate function	Associated Parameters
1	Convolution	(32, 14, 14, 10)	4 × 4 × 4	2	Leaky ReLU	Alpha = 0.2
2	Dropout	(32, 14, 14, 10)	–	–	–	Rate = 0.25
3	Convolution	(64, 7, 7, 5)	4 × 4 × 4	2	Leaky ReLU	Alpha = 0.2
4	Zero padding	(64, 8, 8, 6)	–	–	–	–
5	Batch Normalization	(64, 8, 8, 6)	–	–	–	Momentum = 0.8
6	Dropout	(64, 8, 8, 6)	–	–	–	Rate = 0.25
7	Convolution	(128, 4, 4, 3)	4 × 4 × 4	2	Leaky ReLU	Alpha = 0.2
8	Batch Normalization	(128, 4, 4, 3)	–	–	–	Momentum = 0.8
9	Dropout	(128, 4, 4, 3)	–	–	–	Rate = 0.25
10	Convolution	(128, 2, 2, 2)	4 × 4 × 4	2	Leaky ReLU	Alpha = 0.2
11	Batch Normalization	(128, 2, 2, 2)	–	–	–	Momentum = 0.8
12	Dropout	(128, 2, 2, 2)	–	–	–	Rate = 0.25
13	Flatten	1024	–	–	–	–
14	Dense	1	–	–	Sigmoid	–

Table 2

Structure of discriminator with associated activate function and hyperparameters.

Layer	Type	Output dimension (channel, width, height, depth)	Kernel size	Stride	Activate function	Associated Parameters
1	Dense	31360	–	–	ReLU	–
2	Reshape	(128, 7, 7, 5)	–	–	–	–
3	Upsampling	(128, 14, 14, 10)	–	–	–	–
4	Convolution	(64, 14, 14, 10)	3 × 3 × 3	1	ReLU	–
5	Batch Normalization	(64, 14, 14, 10)	–	–	–	Momentum = 0.8
6	Upsampling	(64, 28, 28, 20)	–	–	–	–
7	Convolution	(32, 28, 28, 20)	3 × 3 × 3	1	ReLU	–
8	Batch Normalization	(32, 28, 28, 20)	–	–	–	Momentum = 0.8
9	Convolution	(16, 28, 28, 20)	3 × 3 × 3	1	ReLU	–
9	Batch Normalization	(16, 28, 28, 20)	–	–	–	Momentum = 0.8
10	Convolution	(1, 28, 28, 20)	5 × 5 × 5	1	Tanh	–

variance of measurement error in diagonal elements. Note that $Cov(\cdot, \cdot)$ indicates the covariance matrix among the denoted variables (e.g., static or dynamic variables). H denotes the measurement matrix, which consists of either 0 or 1, as shown in Equation (6). The dimension of Kalman gain is $(N_s + N_d) \times N_d$.

$$H = [O_{N_d \times N_s} J_{N_d \times N_d}] = \begin{bmatrix} 0 & \dots & 0 & 1 & \dots & 1 \\ \vdots & \ddots & \vdots & \vdots & \ddots & \vdots \\ 0 & \dots & 0 & 1 & \dots & 1 \end{bmatrix}_{N_d \times (N_s + N_d)} \quad (6)$$

where O stands for a zero matrix and J represents an all-ones matrix. The subscripts describe the dimension of the corresponding matrix. The measurement matrix is mathematically designed to select the subset of C_y^p . For example, $C_y^p H^T$ becomes covariance matrix between static and dynamic variables, whereas $H C_y^p H^T$ is covariance matrix among dynamic variables.

2.3. Generative adversarial network (GAN)

GAN consists of two neural networks: discriminator and generator (Goodfellow et al., 2014; Denton et al., 2015). Radford et al. (2015) demonstrate GAN for high-resolution image generation by combining a convolutional neural network (LeCun et al., 1989) and advanced regularization methods, such as dropout (Srivastava et al., 2014). Radford et al. (2015) also demonstrate that batch normalization (Loffe and Szegedy, 2015) helps GAN stabilize the training process, resulting in less initialization sensitivity and prevention of vanishing gradient problem (Pascanu et al., 2013). The generator, G_θ , maps a latent random vector, z , to an image. The latent random vector are not directly observed, but they are inferred implicitly through the trained generator. The discriminator, D_ψ , maps an image to the likelihood, between 0 (fake) and 1 (real), indicating that the image is real (i.e., having geometric features of training data). Note that the input image is from either

training data or realizations of generator in the training process. Also, θ and ψ indicate the associated trained model parameters, weights and biases inside generator and discriminator, respectively. Generator and discriminator are trained adversarially by optimizing the following loss function:

$$\min_{\theta} \max_{\psi} L(\psi, \theta) = \mathbb{E}_h [\log D_\psi(\mathbf{h})] + \mathbb{E}_z [\log(1 - D_\psi(G_\theta(z)))] \quad (7)$$

where \mathbf{h} denotes images drawn from the training dataset and $G_\theta(z)$ stands for realizations from the generator.

In optimizing the trainable parameters of the GAN (i.e., θ and ψ), rectified Adam (Liu et al., 2020) is implemented with the learning rate of 0.0001 and the momentum term (β_1) of 0.5, which is heuristically derived as optimal for the study through the hyperparameter tuning process (Radford et al., 2015). Moreover, the neural network models are designed and implemented on the platform of Python TensorFlow.

We use GAN for a dimensionality reduced parameterization of the high-dimensional subsurface model. Recall that the static variable, $m^s \in \mathbb{R}^{N_s}$, represents the rock properties of interest (e.g., discretized permeability by grid cells), where N_s is extremely large. Using multiple rule-based models as training data, $G_\theta(z)$ enable parameterization of m^s with the latent random vector $z \in \mathbb{R}^{N_z}$, where $N_z \ll N_s$. Typically, N_z is 100, but we can adjust the dimension of z adaptively with a given training dataset. Moreover, z follows a standard normal distribution with zero mean and unit variance. In other words, we train $G_\theta(z)$ so that we can represent a subsurface model by $m^s = G_\theta(z)$, with z parameters.

Fig. 6 shows the schematic diagram of the GAN trained with the ensemble of rule-based models. With a trained generator, the latent random vector enables navigation of the range of possible subsurface models. In other words, we can create various realizations by updating the latent random vector, and each realization has the necessary, realistic features of rule-based models. In this study, 40,000 rule-based models are used for 50,000 epochs with 40 batch sizes, requiring

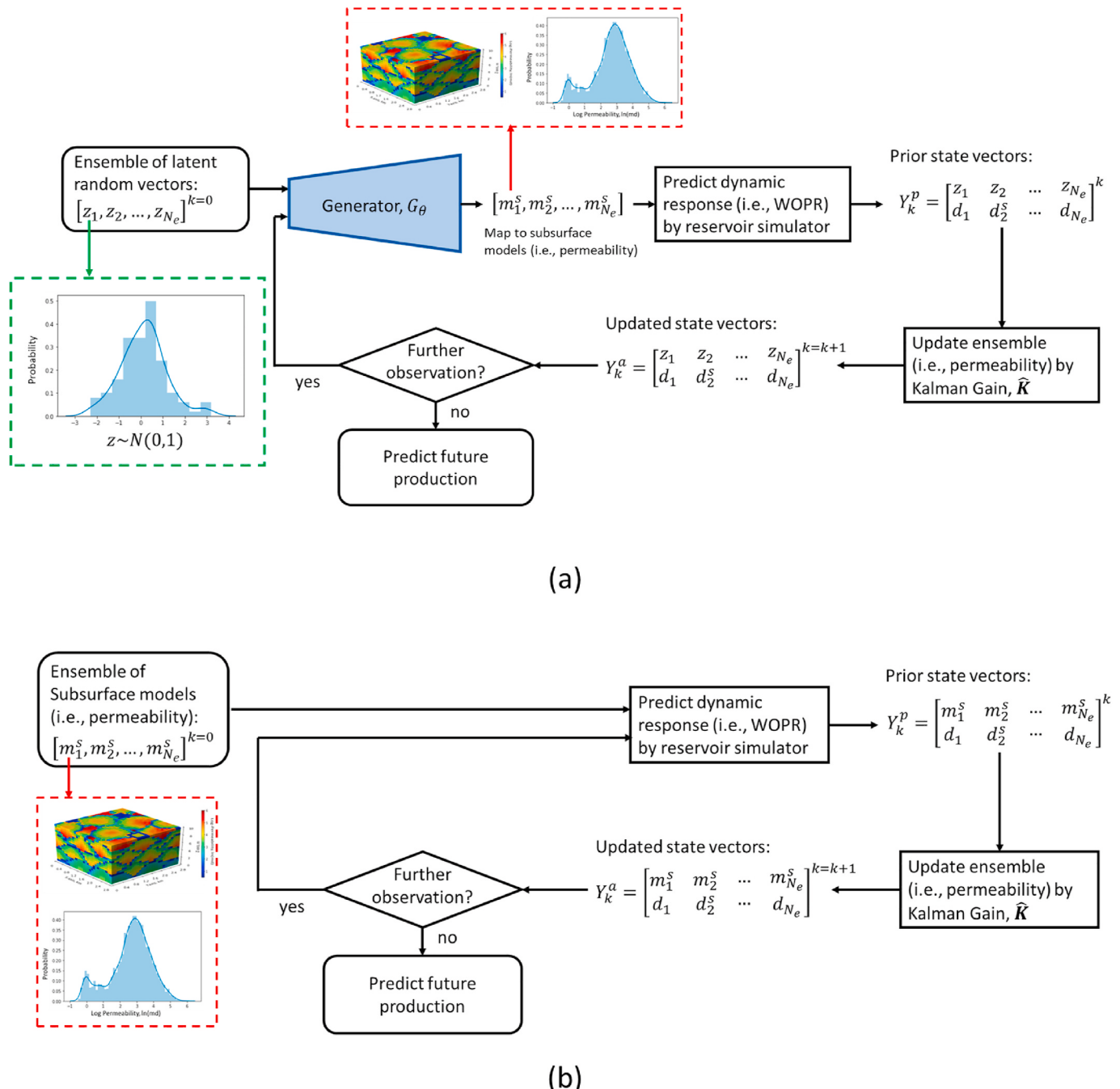


Fig. 8. The workflow of (a) the proposed workflow, GAN-EnKF, and (b) EnKF. Images in red and green dashed boxes show the subsurface models (i.e., permeability) and latent random vector (i.e., z) of the first ensemble member, respectively. Note that the key idea of GAN-EnKF is updating the latent random vector of the ensemble, instead of updating the subsurface model directly. (For interpretation of the references to colour in this figure legend, the reader is referred to the Web version of this article.)

about 8 h on a desktop computer with an environment of CPU Intel E5-1650 3.60 GHz (six processor units) and GPU NVIDIA Quadro M6000 24 GB. The stop criterion in training GAN is determined by visual inspection. As no significant improvement in realizations is observed after 50,000 epochs, we utilize a trained generator for 50,000 epochs. For deployment, the trained GAN generates approximately 1000 realizations per second.

Fig. 7 shows the neural network structure of the generator. First, the generator maps a latent random vector (100 elements) in the input layer to a hidden layer of 31,360 elements in a fully-connected manner. The next operation reshapes the hidden layer to a feature map of $7 \times 7 \times 5$ (i.e., width \times length \times height) dimension with 128 channels. The

individual channels, depth of image, contains a different piece of information in the feature map. For the remainder of the operations, the feature map's dimension increases while the number of channels decreases. At the last feature map, the generator produces a 3D model (i.e., subsurface model) of $28 \times 28 \times 20$ that is identical to the dimension of the rule-based model. The dimensions of feature maps and the number of channels should be updated according to the size of the subsurface model. Table 1 and Table 2 represent the detailed structure of the generator and discriminator, respectively, including the activation functions and convolutional neural network hyperparameters.

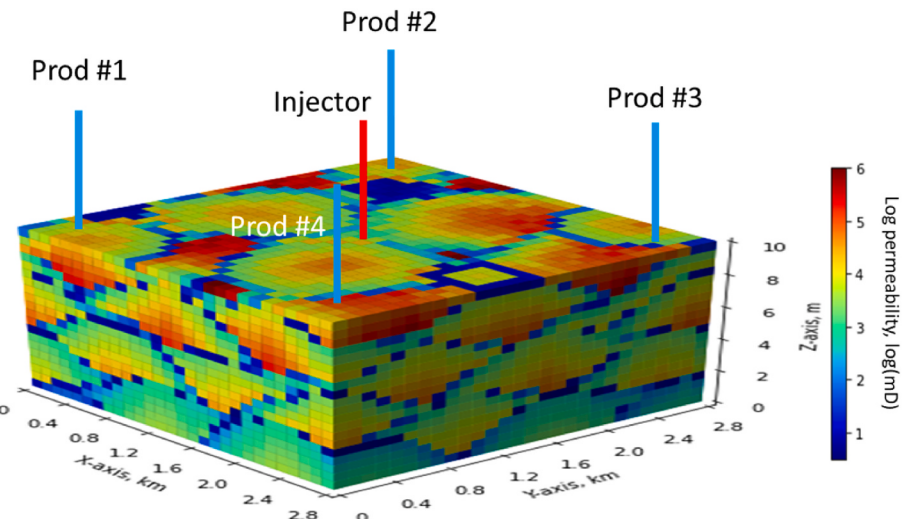


Fig. 9. The reference subsurface permeability model with the well locations. Note that permeability is visualized in a log-scale.

Table 3
Detailed reference subsurface model conditions.

Reservoir description	Values
Reservoir extent	2.8 km × 2.8 km × 10 m
Grid system	28 × 28 × 20 grid cells
Grid cell dimension	100 m × 100 m × 0.5 m
Top depth, ft	10,000
Initial pressure, psi	8000
Initial water saturation, fraction	0.15
Average porosity, fraction	0.2
Average permeability, mD	25.5
Standard deviation of permeability, mD	29.9
Dykstra-Parsons coefficient	0.741
Well pattern	Inverted-five spot (one injector and four producers)
Producer location, grid coordinate	(3, 3), (3, 25), (25, 3), and (25, 25)
Injector location, grid coordinate	(14, 14)
Producer BHP control, psi	5000
Injector BHP control, psi	35,000

2.4. GAN-EnKF

The proposed method, GAN-EnKF, combines EnKF with the parametrization through the GAN trained with the rule-based models. Fig. 8 shows the workflow comparison between GAN-EnKF and typical EnKF. The plots in red and green boxes represent the distribution of permeability and latent random vector from an initial ensemble member, respectively. Typical EnKF update permeability models of the ensemble directly. GAN-EnKF, however, assimilates the observed fluid production data to the latent random vectors and transforms the updated latent random vector to permeability model through $G_\theta(\cdot)$. The converted permeability is input to a reservoir simulator to predict corresponding dynamic responses (e.g., fluid flow rates) to continue the iterative assimilation in the EnKF. GAN-EnKF has two main advantages over the current fluid production integration workflow with EnKF. First, as $N_z \ll N_s$, due to the dimensionality reduction of convolutional neural networks, improving the computational efficiency for computing \hat{K} and updating state vectors. Moreover, unlike commonly observed bimodal (or multi-modal) permeability distributions, the latent random vector follows a standard normal distribution, which is compatible with a critical mathematical assumption of EnKF. As such, GAN-EnKF effectively prevents possible artifacts, such as filter divergence (i.e., the collapse of variability among ensemble) and overshooting (i.e., unrealistically high or low permeability), which often occurs in applying EnKF to bimodal properties.

3. Result

We demonstrate our proposed GAN-EnKF workflow for production data integration with an ensemble of 3D rule-based subsurface deep-water lobe depositional system models and a single truth model. The truth model is an exhaustive permeability model representing the inaccessible natural, which is consistent with the geological concepts in the ensemble and is applied with the physics-based fluid flow simulation model to calculate the observed measurements of fluid production at wells. We describe the truth subsurface model and an initial ensemble of rule-based models (section 3.1.), show the history matching results (section 3.2.), and verify the quality of the result through a statistical assessment (section 3.3).

3.1. Reference subsurface model and initial ensemble

The reference (i.e., truth) subsurface model is calculated with the rule-based modeling method. Fig. 9 shows the reference permeability model and well locations. For running a reservoir simulation, we discretize the reference subsurface model with $28 \times 28 \times 20$ grid cells in x-, y-, and z-direction, and each grid cell is $100 \times 100 \times 0.5$ m in size. Lobe radius and thickness are 750 m and 4 m, respectively. The two rock facies are sand preferentially located in the center of the lobe elements, while shale is preferentially located along the margins on the top of lobe elements. Water is injected through an injection well in the center of the reservoir, and four producing wells are positioned at each corner of the model to produce oil. The injector and producers are operated at constant bottom hole pressure. Table 3 lists the specific conditions of the reference subsurface model. The observed measurements from the reference model, well oil production rates (WOPR) from four producers at 100, 200, 300, 400, and 500 days are applied to update the permeability state vector over the ensemble. Then future production is predicted up to 2500 days. We assume reservoir models' porosity homogenous and identical over the ensemble, so only permeability is assimilated by the production history.

The ensemble consists of 100 realizations. Initial realizations of the ensemble are generated with the same rule-based modeling method and geological assumptions (e.g., stacking pattern and lobe dimension) as the reference subsurface model. The realizations are conditioned to hard data (i.e., observed permeability samples at well locations) through semantic inpainting following Jo et al. (2020). Fig. 10 shows three

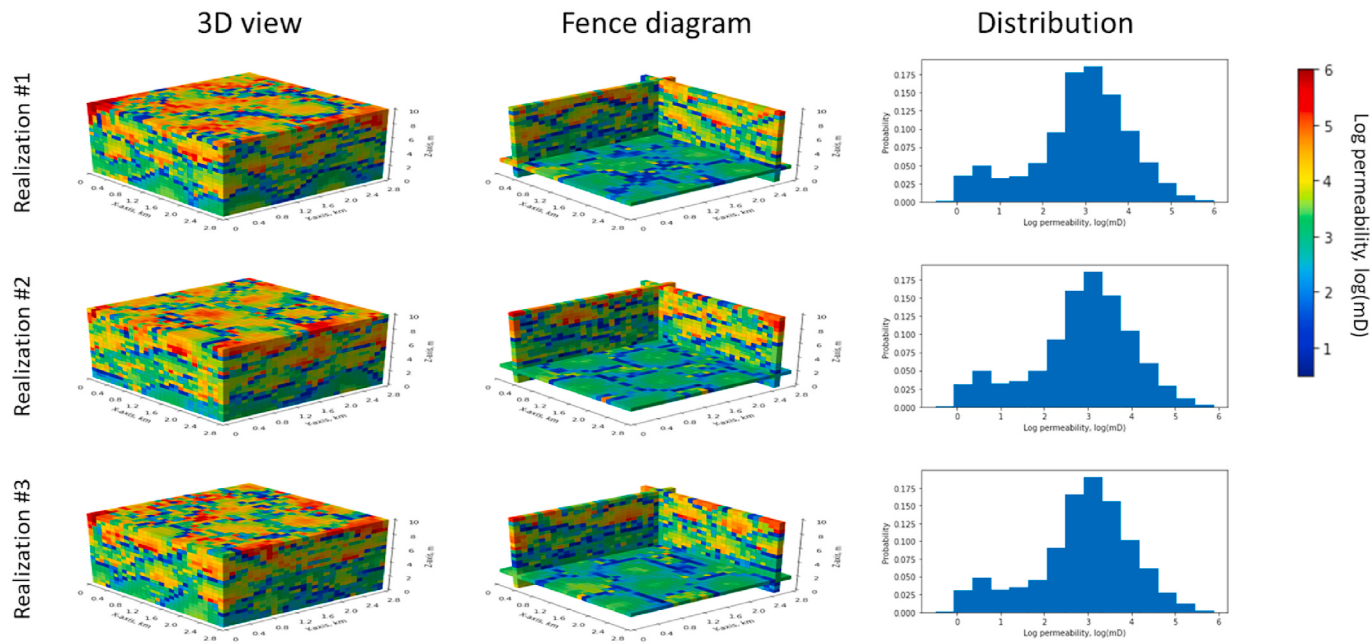


Fig. 10. Initial permeability realizations in the ensemble. Permeability is on a log-scale.

permeability realizations out of 100 from the ensemble. Reservoir fluid flow simulation predicts WOPR of the ensemble at 100, 200, 300, 400, and 500 days, and the permeability realizations of the ensemble are updated by the misfits between the predicted fluid production and the observed measurements of production history at the four producing wells through Equation (4).

3.2. GAN-EnKF

Fig. 11 shows the updated realizations of GAN-EnKF and the previous EnKF method. In Fig. 11, each row indicates individual realization. Moreover, the first, second, and third columns of subplots in Fig. 11 are 3D view, fence diagrams, and histograms of permeability in each realization. The updated ensemble through GAN-EnKF conserves the geological characteristics observed in the ensemble of initial rule-based models. Important geological features such as hierarchical trends, lobe geometries, and shaly boundaries of lobes are preserved in all realizations of Fig. 11(a). In comparison, EnKF fails to preserve these geological features in the updated realizations, as shown in Fig. 11(b). For example, shaly boundaries of lobes on top of lobe elements are smeared with sandy facies. Moreover, the hierarchical trends in the initial realizations are not preserved in the updated models shown in Fig. 11(b). Moreover, the permeability distributions of the updated realizations through GAN-EnKF preserves bimodal distribution, consistent with the true reservoir model and the initial ensemble. In contrast, the updated ensemble of EnKF approaches the Gaussian distribution in permeability due to the Gaussian assumption, resulting in indistinguishable rock types and smeared lobe boundaries.

Cell-by-cell average and standard deviation of permeability over the ensemble are visualized in Figs. 12 and 13. Even though the individual reservoir model in the initial ensemble shows the clear lobe boundaries (in Fig. 10), the average permeability rarely shows the boundaries due to high variability among the initial ensemble, as shown in Fig. 12(a). GAN-EnKF effectively reduces the variability among the ensemble in the assimilation process, resulting in relatively distinguishable lobe boundaries in Fig. 12(b). However, the updated ensemble of EnKF shows no significant reduction in the variability among the ensemble; thereby, no clear lobe boundaries in Fig. 12(c). Moreover, the standard deviations of permeability do not show a significant difference between the

initial ensemble and the updated ensemble of EnKF, as presented in Fig. 13(a) and (c). In contrast, the updated ensemble of GAN-EnKF shows lower standard deviations in the centers of lobes, as shown in Fig. 13(b).

Fig. 14 presents the WOPR prediction of GAN-EnKF and EnKF. Red, light gray, and dark gray lines are reference, before-, and after-assimilation of production history into the ensemble, respectively. The initial ensemble prediction has a wide range of fluid flow predictions for four producing wells. Fig. 14(a) demonstrates that GAN-EnKF reduces the uncertainty of the ensemble with improving accuracy with the observed measurements. Note that only 500 days of observed oil production measurements are utilized to update the initial rule-based ensemble, and the remaining 2000 days of production are predicted with the updated ensemble applied to the physics-based fluid flow simulation model. Moreover, both EnKF and GAN-EnKF assimilate production history to the ensemble by five-time iterative updates at 100, 200, 300, 400, and 500 days of production. Even though the proposed GAN-EnKF method slightly underestimates WOPR in producer #3, the results are reliable by capturing the observed measurements within the ensemble-based uncertainty model range. The EnKF significantly underestimates the WOPR of producer #1 and #3 while overestimating that of producer #2 and #4, and the uncertainty range of the updated ensemble is too narrow; therefore, the uncertainty model is neither accurate nor precise, as shown in Fig. 14(b).

Fig. 15 visualizes the cumulative oil production at each producer. GAN-EnKF correctly updates the ensemble to fit the reference not only for 500 days (i.e., the interval of observed measurements assimilated to update the ensemble of models) but also for the entire 2500 days. EnKF fails to match the observed measurements, 500 days of cumulative oil production. Fig. 15(b) shows that cumulative oil production prediction of the updated ensemble by EnKF increases in error with respect to the observed measurement over production time, which may lead to sub-optimum development decision making. Table 4 shows the cumulative oil production by P10, P50, P90 for the EnKF updated ensemble, and none of the predicted production range (i.e., between P10 and P90) includes the observed measurements. GAN-EnKF successfully predicts future cumulative production except for producer #3. While the production of producing well #3 is above P90, the error of GAN-EnKF is significantly less than that of EnKF, and it is anticipated that further

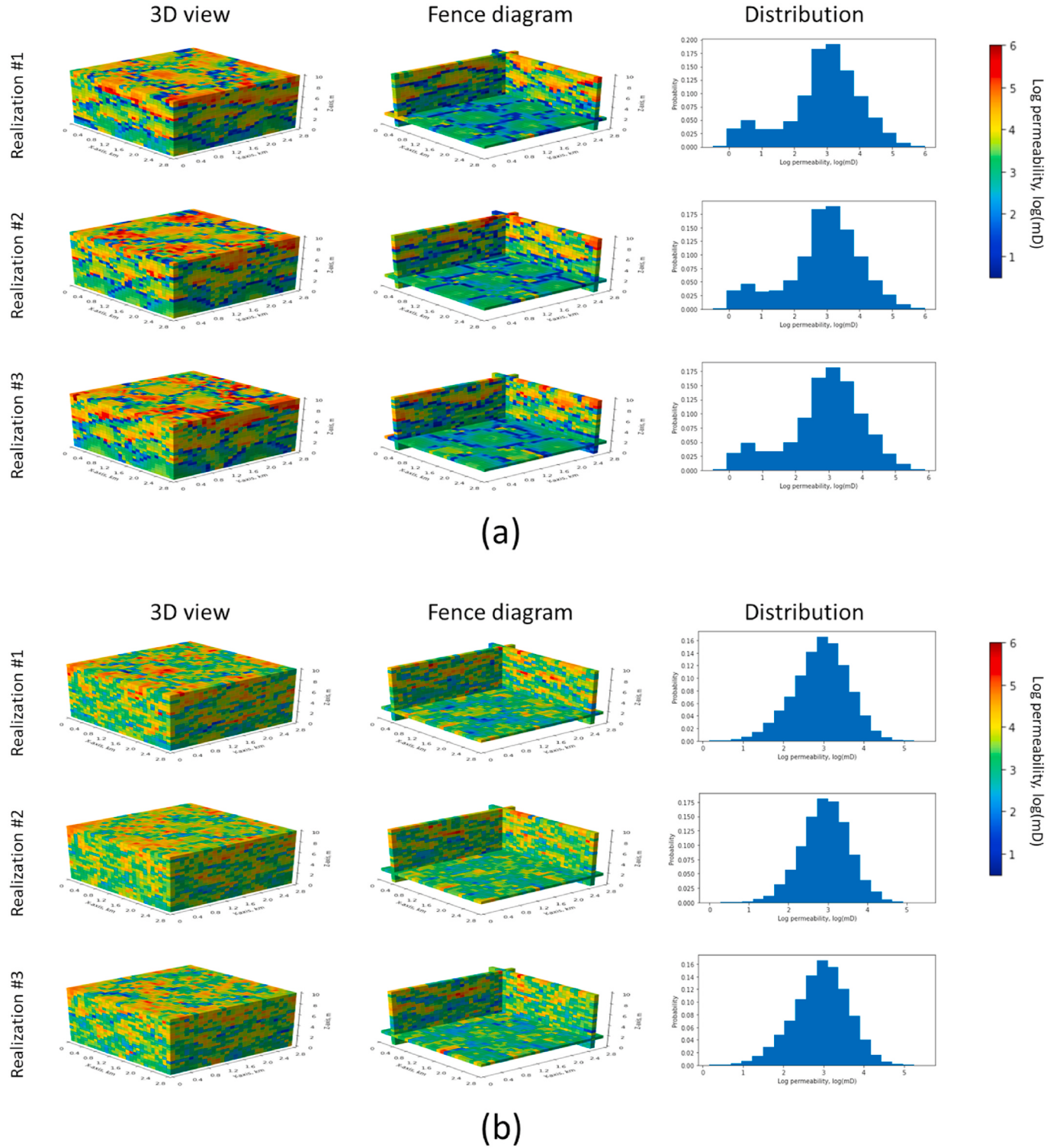


Fig. 11. Updated permeability realizations in the ensemble: (a) GAN-EnKF and (b) EnKF. Permeability is on a log-scale.

assimilation of production history will reduce this error.

Fig. 16 shows the pressure of grid blocks in four production wells' locations. Unlike production forecasts, grid block pressure is inaccessible in real field development but only calculated from reservoir simulation. However, grid block pressure is still useful to evaluate the performance of the history matching. The initial ensemble shows wide uncertainty ranges of pressure predictions for all four wells. GAN-EnKF successfully reduces the uncertainty while enhancing precision in pressure forecasts, as shown in Fig. 16(a). In contrast, EnKF shrinks the

uncertainty ranges too excessively, and the forecasts of the updated ensemble is imprecise, deviate from the reference pressure in Fig. 16(b). In short, grid block pressure shows a consistent result with oil production.

Table 5 shows the computation time for updating the ensemble. The dimension of the state vector for EnKF is much larger than for GAN-EnKF (i.e., $N_z \ll N_s$), resulting in a reduction in cost by 99.95%. Note that computational time in training GAN is not included in Table 5. However, this reduction in computational cost increases as the model size

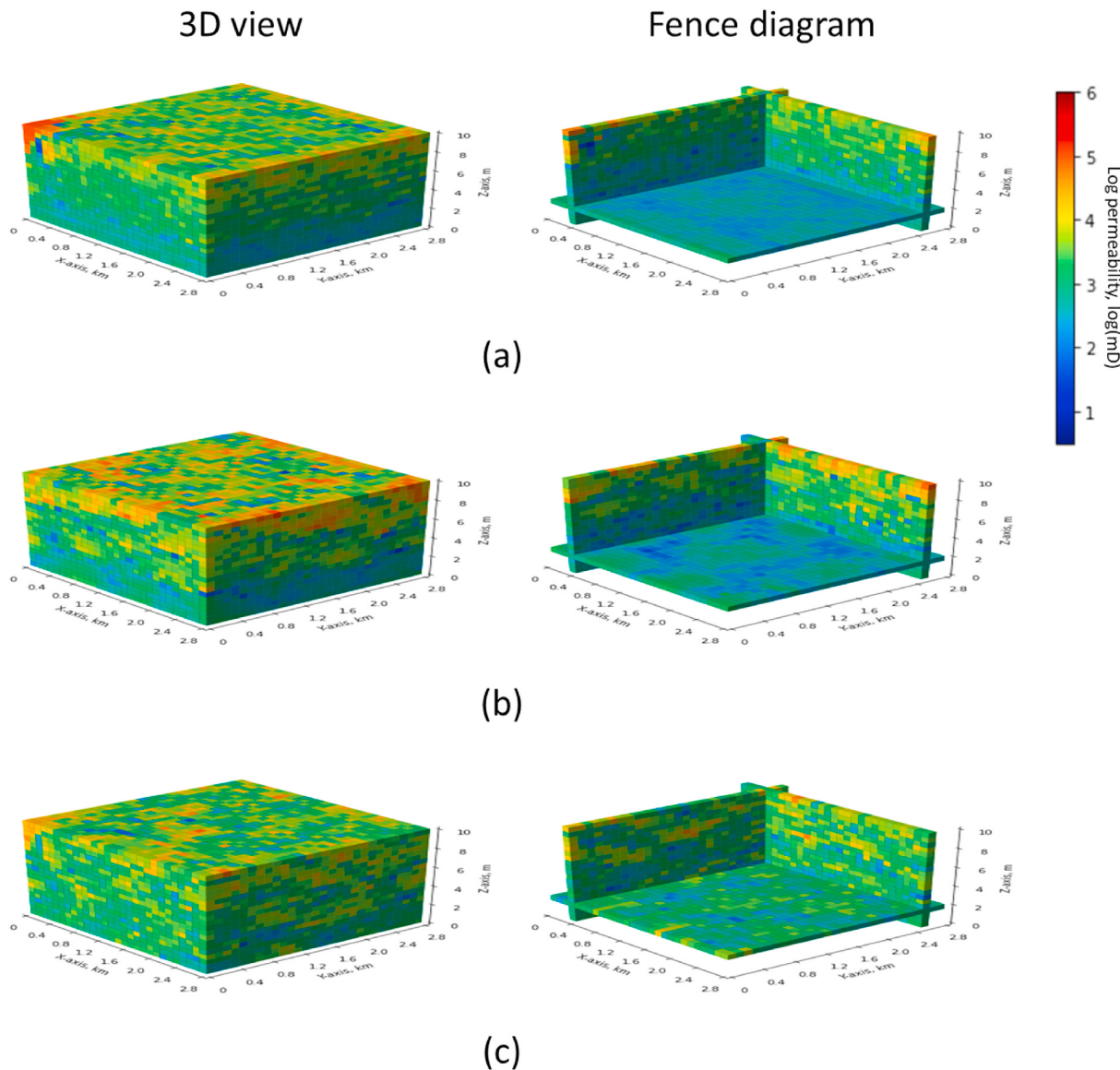


Fig. 12. Cell-by-cell average permeability over ensemble: (a) initial ensemble, (b) updated ensemble of GAN-EnKF, and (c) updated ensemble of EnKF. Permeability is on a log-scale.

increases or the iterations to update the ensemble increase. As the computational complexity in EnKF is $O(N_s^2 \cdot N_d)$ (Majda and Tong, 2018), the computational time increases by the second-order of the subsurface model's dimension. For example, in a larger subsurface model, whose dimension is $128 \times 128 \times 32$ in x-, y-, and z-direction, the computational time in updating the ensemble will be roughly 1000 times more for a one-step update than this demonstration. As we update five times in this study, the computational time increase due to the large subsurface dimension will eventually exceed the additional computation time in training GAN.

3.3. Quality assessment

We perform a quantitative assessment for the performance of the proposed GAN-EnKF method by visualizing the pre-assimilation and post-assimilation ensemble of models in a projected 2D space with multidimensional scaling (MDS). MDS is a visualization technique that measures the pairwise distances (i.e., dissimilarity) between individual samples and maps them to 2D (Borg and Groenen, 1997; Caers, 2011; Tan et al., 2014). Fig. 17 shows the MDS plot of subsurface model realizations (each point is an actual subsurface model in the ensemble).

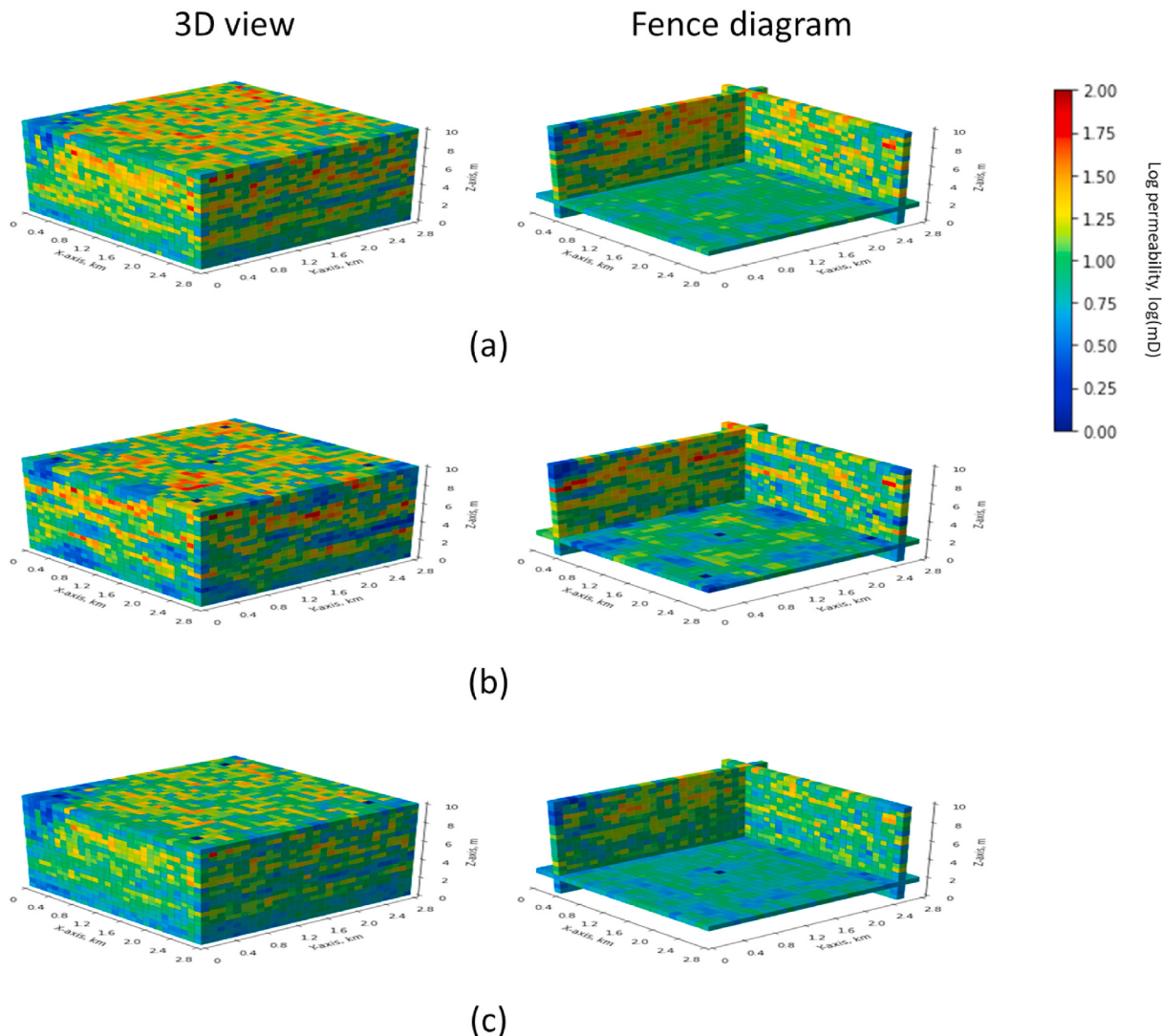


Fig. 13. Cell-by-cell standard deviation of permeability over ensemble: (a) initial ensemble, (b) updated ensemble of GAN-EnKF, and (c) updated ensemble of EnKF. Permeability is on a log-scale.

Red, light-gray, and dark gray points are reference subsurface model, initial realizations, and updated realizations, respectively. The distance between models denotes the level of model pairwise dissimilarity. The initial ensemble has a wide range in the MDS plot. GAN-EnKF updates the ensemble closer to the reference, reducing the model to model dissimilarity. EnKF fails to decrease the between model variability, and the centroid of the updated ensemble generally does not approach reference. The proposed GAN-EnKF method uncertainty model is more accurate and precise.

In addition, we analyze the proposed GAN-EnKF method and EnKF updated ensembles with the method of analysis of distance (ANODI), similar to Tan et al. (2014). Instead of Jensen-Shannon divergence, we compute the average square difference (i.e., MSE) between realizations as a distance measurement. Two distances, within- and between-distance, are defined through Equations (8) and (9). Within-distance denotes the diversity of the ensemble, while between-distance indicates inconsistency with the reference. In the adequately updated ensemble, both within- and between-distance

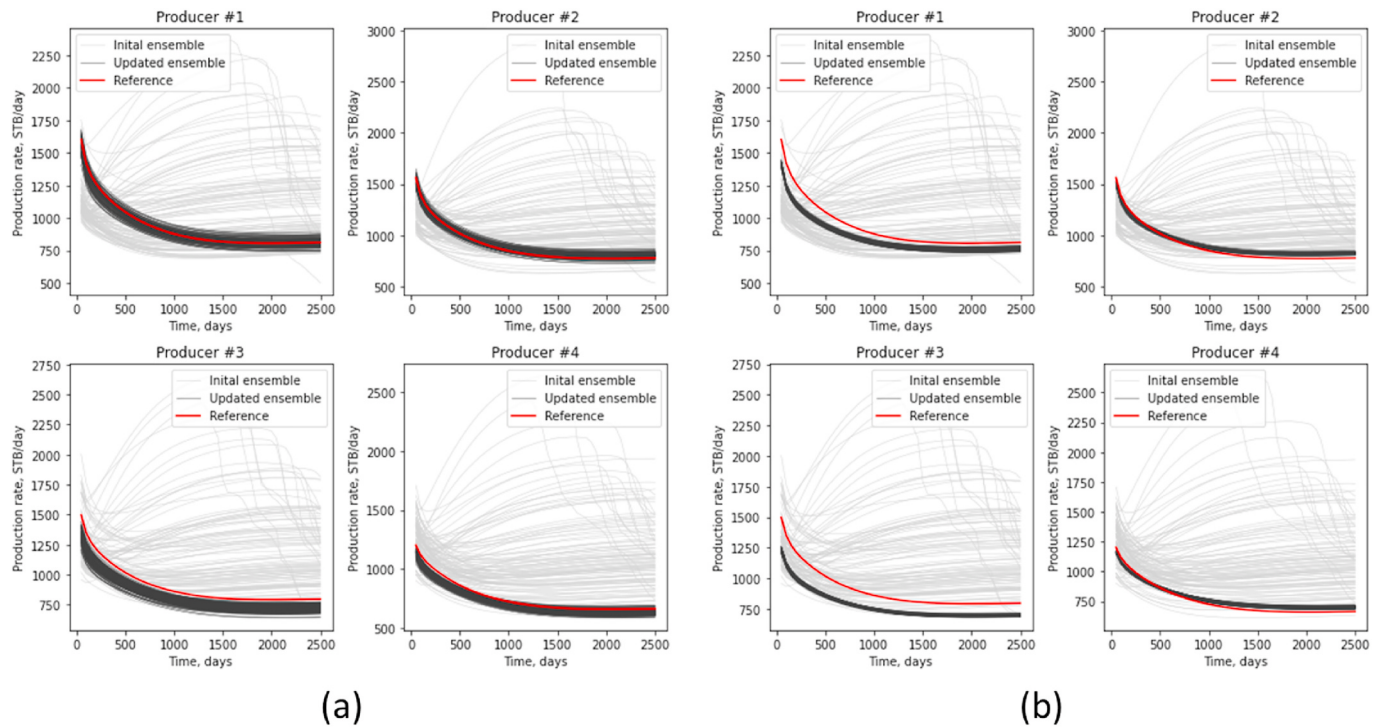


Fig. 14. WOPR prediction of ensembles: (a) GAN-EnKF and (b) EnKF. Red, light gray, and dark gray lines are reference, before-, and after-assimilation of the ensemble, respectively. (For interpretation of the references to colour in this figure legend, the reader is referred to the Web version of this article.)

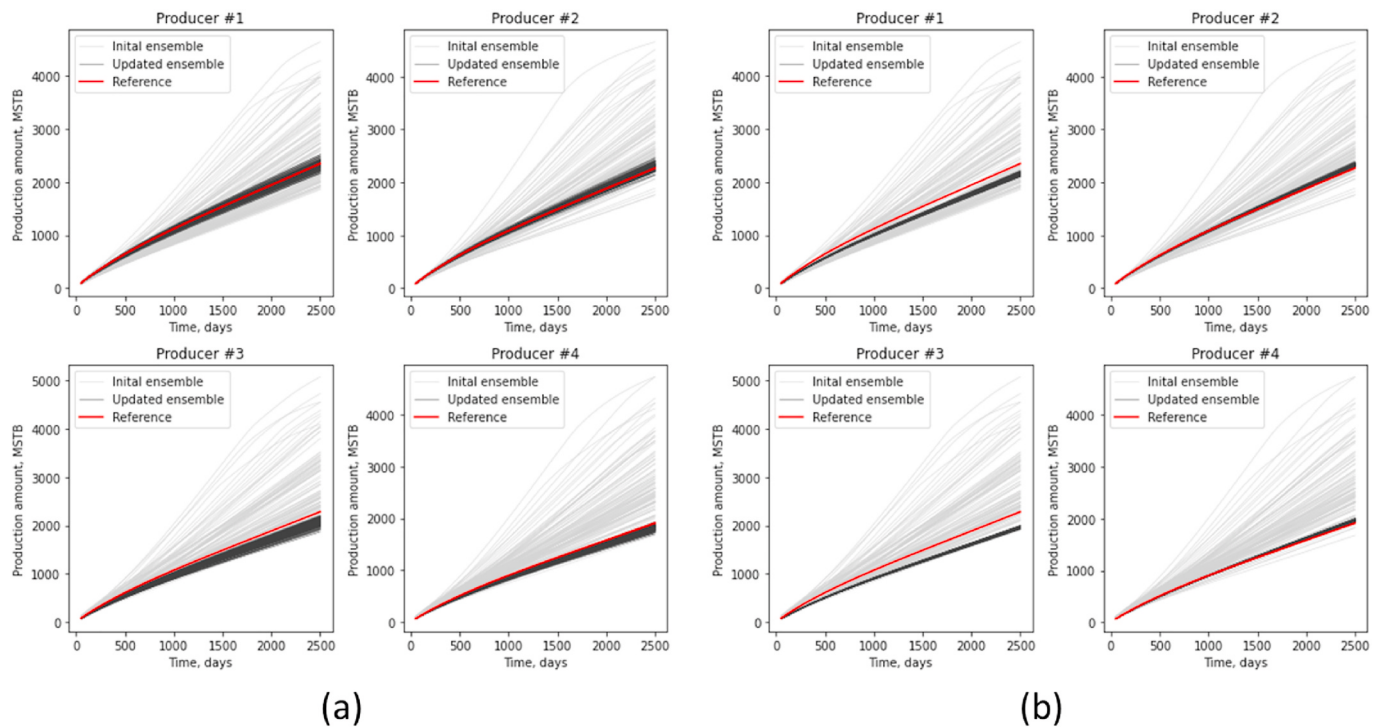


Fig. 15. Cumulative oil production prediction of ensembles: (a) GAN-EnKF and (b) EnKF. Red, light gray, and dark gray lines are reference, before-, and after-assimilation of the ensemble, respectively. (For interpretation of the references to colour in this figure legend, the reader is referred to the Web version of this article.)

Table 4

Cumulative oil production from each well at 2500 days. The unit is MSTB.

	GAN-EnKF			EnKF			True
	P10	P50	P90	P10	P50	P90	
Producer #1	2219	2331	2422	2137	2169	2193	2346
Producer #2	2223	2305	2393	2306	2333	2360	2269
Producer #3	1982	2067	2162	1934	1954	1979	2284
Producer #4	1759	1826	1920	1948	1970	1994	1910

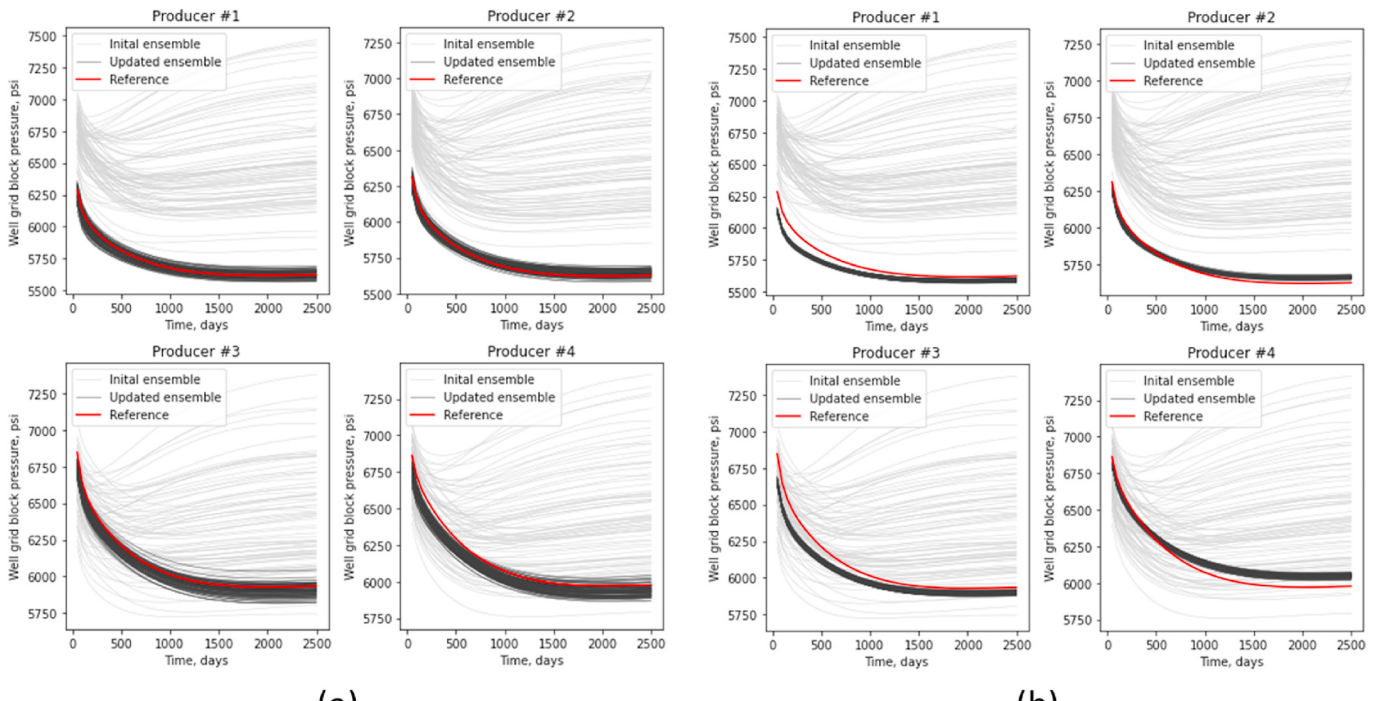


Fig. 16. Grid pressure prediction of ensembles: (a) GAN-EnKF and (b) EnKF. Red, light gray, and dark gray lines are reference, before-, and after-assimilation of the ensemble, respectively. (For interpretation of the references to colour in this figure legend, the reader is referred to the Web version of this article.)

should decrease.

$$d_{\text{within}} = \frac{1}{N_e(N_e - 1)} \sum_{i=1}^{N_e} \sum_{i'=1}^{N_e} \frac{[m_i^s - m_{i'}^s]^2}{N_{\text{grid}}} \quad (8)$$

$$d_{\text{between}} = \frac{1}{N_e} \sum_{i=1}^{N_e} \frac{[m_i^s - m_{\text{ref}}^s]^2}{N_{\text{grid}}} \quad (9)$$

where m_i is the array of subsurface properties (i.e., log-permeability) of

i^{th} realization in the ensemble and m_{ref} is the array of the reference properties. N_{grid} is the number of grid cells in the subsurface model.

Table 6 shows ANODI scores of both the initial and updated ensemble. The initial ensemble scored 0.292 in variability among realizations and 0.313 in inconsistency with the reference. GAN-EnKF updates the ensemble to have less diversity and inconsistency than the initial, indicating successful assimilation of observed measurement. EnKF increases the inconsistency, indicating more inaccuracy than the initial ensemble. Even though EnKF reduces diversity, the uncertainty

Table 5

Computation time to update the ensemble, with an environment of CPU Intel E5-1650 3.60 GHz. Note that this computation time excludes the computational time in training GAN.

Methods	Computation time, sec	Ratio
EnKF	3.797	100%
GAN-EnKF	0.00196	0.05%

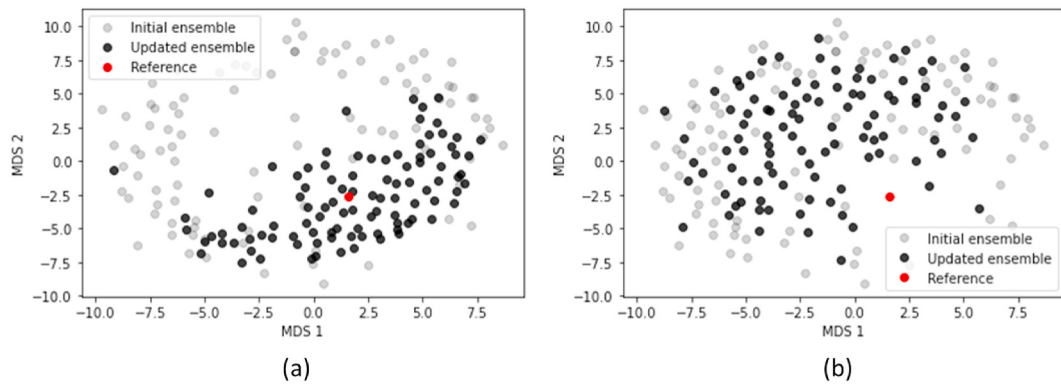


Fig. 17. MDS plot of realizations of (a) GAN-EnKF and (b) EnKF. Red, light-gray, and dark gray points indicate reference subsurface model, initial realization, and updated realizations, respectively. The distance among points denotes the level of similarity, e.g., the more similar, the closer. (For interpretation of the references to colour in this figure legend, the reader is referred to the Web version of this article.)

Table 6
ANODI scores of the initial and updated ensemble.

Methods	Inconsistency	Diversity
Initial ensemble	0.313	0.292
Updated ensemble (GAN-EnKF)	0.278	0.212
Updated ensemble (EnKF)	0.318	0.276

model is imprecise.

4. Conclusion

By parametrizing high-dimensional reservoir properties through the GAN, we introduce a method to assimilate physics-based dynamic information into realistic subsurface model realizations for fluid production history in a complicated deepwater lobe reservoir. GAN enables effective dimensionality reduction and efficient realization calculation of the subsurface model once trained. Moreover, the generator's input, a latent random vector, follows a standard normal distribution, compatible with a fundamental assumption of EnKF. Therefore, GAN-EnKF outperforms EnKF in the accuracy of prediction, the preservation of geological features, and computational efficiency for updating the ensemble. Possible future work includes: (1) expanding the uncertainty model by conditioning subsurface models with different geological

scenarios through conditional GAN, (2) broadening this application to the different depositional settings, such as a fluvial or deltaic reservoir, and (3) applying GAN-EnKF for additional data integration. Especially in training GAN and implementing EnKF, no additional constraint is required depending on data types (e.g., bottom-hole pressure, production rates, and other dynamic responses) or geological structures in reservoir models, indicating that GAN-EnKF is readily available for different reservoir types.

Declaration of competing interest

The authors declare that they have no known competing financial interests or personal relationship that could have appeared to influence the work reported in this paper.

Acknowledgments

The authors thank the reviewers for their critical feedback and their help to improve the quality of the manuscript. Appreciation the support of the DIRECT consortium for subsurface data analytics and machine learning at The University of Texas at Austin. The corresponding author is also thankful to the Hildebrand Department of Petroleum and Geosystems Engineering at the University of Texas at Austin, Texas, USA.

Nomenclatures

y	State vector
m^s	Static variables
d	Dynamic response
Y	State matrix
\bar{Y}	Mean of static vector
D_{obs}	Observed data
N_e	Number of ensemble members
N_s	Dimension of static variables
N_{grid}	The number of grid cells
N_d	Dimension of dynamic responses
N_z	Dimension of latent random vector
\hat{K}	Kalman gain
C_y	Estimate error covariance
C_D	Measurement precision matrix
$Cov(\cdot, \cdot)$	Covariance matrix
H	Measurement matrix
h	Image from training dataset
z	Latent random vector

$D_\psi(\cdot)$	Discriminator of GAN
$G_\theta(\cdot)$	Generator of GAN

Subscripts

k	kth time step
i	ith ensemble member
e	Ensemble
s	Static properties
d	Dynamic properties
ψ	Weights in discriminator
θ	Weights in generator
ref	reference

Superscripts

a	Assimilation
p	Pre-assimilation
T	Transpose
s	Static properties

Credit author statement

Honggeun Jo: Methodology, Conceptualization, Formal analysis, Software, Investigation, Visualization, Validation, Writing - original draft. Wen Pan: Data Curation, Investigation. Javier E. Santos: Visualization, Investigation. Hyungsik Jung: Software, Investigation. Michael J. Pyrcz: Supervision, Investigation, Writing- Reviewing and Editing,

References

- Abreu, V., Sullivan, M., Pirmez, C., Mohrig, D., 2003. Lateral accretion packages (LAPs): an important reservoir element in deep water sinuous channels. *Mar. Petrol. Geol.* 20 (6–8), 631–648.
- Bertoncello, A., Sun, T., Li, H., Mariethoz, G., Caers, J., 2013. Conditioning surface-based geological models to well and thickness data. *Math. Geosci.* 45 (7), 873–893.
- Borg, I., Groenen, P., 1997. Modern Multidimensional Scaling: Theory and Applications. Springer, New York.
- Caers, J., 2011. Modeling Uncertainty in the Earth Sciences. Wiley-Blackwell, New York.
- Canchumuni, S.W., Castro, J.D., Potratz, J., Emerick, A.A., Pacheco, M.A.C., 2020. Recent developments combining ensemble smoother and deep generative networks for facies history matching. *Comput. Geosci.* 25, 433–466. <https://doi.org/10.1007/s10596-020-10015-0>.
- Chan, S., Elsheikh, A.H., 2019. Parametric generation of conditional geological realizations using generative neural networks. *Comput. Geosci.* 23, 925–952. <https://doi.org/10.1007/s10596-019-09850-7>.
- Chang, H., Zhang, D., Lu, Z., 2019. History matching of facies distribution with the EnKF and level set parameterization. *J. Comput. Phys.* 229 (20), 8011–8030. <https://doi.org/10.1016/j.jcp.2010.07.005>. ISSN 0021-9991.
- Cho, Yongchae, 2021. Stochastic discrete fracture network modeling in shale reservoirs via integration of seismic attributes and petrophysical data. *Interpretation* 9 (4), 1–50. <https://doi.org/10.1190/int-2020-0210.1>. In press.
- Cho, Y., Gibson Jr., R.L., Zhu, D., 2018. Quasi 3D transdimensional Markov-chain Monte Carlo for seismic impedance inversion and uncertainty analysis. *Interpretation* 6 (3), T613–T624.
- Cojan, I., Fouché, O., Lopéz, S., Rivoirard, J., 2005. Process-based reservoir modelling in the example of meandering channel. In: Leuangthong, O., Deutsch, C.V. (Eds.), Geostatistics Banff 2004, Quantitative Geology and Geostatistics, vol. 14. Springer, Dordrecht.
- Denton, E.L., Chintala, S., Fergus, R., 2015. Deep generative image models using a laplacian pyramid of adversarial networks. *Adv. Neural Inf. Process. Syst.* 1486–1494.
- Deptuck, M.E., Piper, D.J., Savoye, B., Gervais, A., 2008. Dimensions and architecture of late Pleistocene submarine lobes off the northern margin of East Corsica. *Sedimentology* 55 (4), 869–898. <https://doi.org/10.1111/j.1365-3091.2007.00926.x>.
- Emerick, A.A., Reynolds, A.C., 2012. Combining the ensemble Kalman filter with Markov-Chain Monte Carlo for improved history matching and uncertainty characterization. *SPE J.* 17, 418–440. <https://doi.org/10.2118/141336-PA>.
- Evensen, G., 1994. Sequential data assimilation with a nonlinear quasi-geostrophic model using Monte Carlo methods to forecast error statistics. *J. Geophys. Res.* 99, 10143–10162. <https://doi.org/10.1029/94JC00572>.
- Goodfellow, I.J., Pouget-Abadie, J., Mirza, M., Xu, B., Warde-Farley, D., Ozair, S., Courville, A., Bengio, Y., 2014. Generative adversarial networks. *Adv. Neural Inf. Process. Syst.*
- Jafarpour, B., McLaughlin, D.B., 2008. History matching with an ensemble kalman filter and discrete cosine parameterization. *Comput. Geosci.* 12 (2), 227–244.
- Jo, H., Jung, H., Ahn, J., Lee, K., Choe, J., 2017. History matching of channel reservoirs using ensemble kalman filter with continuous update of channel information. *Energy Explor. Exploit.* 35 (1), 3–23. <https://doi.org/10.1177/0144598716680141>.
- Jo, H., E-Santos, J., Pyrcz, M.J., 2019. Conditioning stratigraphic, rule-Based models with generative adversarial networks: a deepwater lobe, deep learning example. In: Paper Presented at the 2019 AAPG Annual Convention and Exhibition. San Antonio, Texas, USA, 19–22 May 2019. <https://doi.org/10.1306/42402jo2019>.
- Jo, H., Santos, J.E., Pyrcz, M.J., 2020. Conditioning well data to rule-based lobe model by machine learning with a generative adversarial network. *Energy Explor. Exploit.* 38 (6), 2558–2578. <https://doi.org/10.1177/0144598720937524>.
- Jung, H., Jo, H., Kim, S., Lee, K., Choe, J., 2017. Recursive update of channel information for reliable history matching of channel reservoirs using EnKF with DCT. *J. Petrol. Sci. Eng.* 154, 19–37. <https://doi.org/10.1016/j.petrol.2017.04.016>.
- Jung, S., Lee, K., Park, C., Choe, J., 2018. Ensemble-based data assimilation in reservoir characterization: a review. *Energies* 11 (2), 445. <https://doi.org/10.3390/en11020445>.
- Kang, B., Jung, H., Jeong, H., Cheo, J., 2020. Characterization of three-dimensional channel reservoirs using ensemble Kalman filter assisted by principal component analysis. *Petrol. Sci.* 17, 182–195. <https://doi.org/10.1007/s12182-019-00362-8>.
- Katzfuss, M., Stroud, J.R., Wikle, C.K., 2016. Understanding the ensemble kalman filter. *Am. Statistician* 70 (4), 350–357. <https://doi.org/10.1080/00031305.2016.1141709>.
- Kim, S., Lee, C., Lee, K., Choe, J., 2016. Characterization of channelized gas reservoirs using ensemble kalman filter with application of discrete cosine transformation. *Energy Explor. Exploit.* 34 (2), 319–336. <https://doi.org/10.1177/0144598716630168>.
- Laloff, E., Hérault, R., Jacques, D., Linde, N., 2018. Training-image based geostatistical inversion using a spatial generative adversarial neural network. *Water Resour. Res.* 54 (1), 381–406. <https://doi.org/10.1002/2017WR022148>.
- LeCun, Y., Boser, B., Denker, J.S., Henderson, D., Howard, R.E., Hubbard, W., Jackel, L.D., 1989. Backpropagation applied to handwritten zip code recognition. *Neural Comput.* 1, 541–551.
- Loffe, E., Szegedy, C., 2015. Batch normalization: accelerating deep network training by reducing internal covariate shift. In: Paper Presented at the 32nd International Conference on Machine Learning. Lille, France, 6–11 July 2015.
- Majda, A.J., Tong, X.T., 2018. Performance of ensemble Kalman filters in large dimensions. *Commun. Pure Appl. Math.* 71 (5), 892–937.
- Michael, H.A., Li, H., Boucher, A., Sun, T., Caers, J., Gorelick, S.M., 2010. Combining geologic-process models and geostatistics for conditional simulation of 3-D subsurface heterogeneity. *Water Resour. Res.* 46 (5), 1–20. <https://doi.org/10.1029/2009WR008414>.
- Moreno, D., Aanonsen, S.I., 2007. Stochastic facies modelling using the level set method. In: Paper Presented at the EAGE Conference on Petroleum Geostatistics. <https://doi.org/10.3997/2214-4609.201403056>. Cascais, Portugal, 10–14 September 2007.
- Mosser, L., Dubrule, O., Blunt, M.J., 2017. Reconstruction of three-dimensional porous media using generative adversarial neural networks. *Phys. Rev.* 96 (4), 043309. <https://link.aps.org/doi/10.1103/PhysRevE.96.043309>.
- Nævdal, G., Mannseth, T., Vefring, E.H., 2002. Near-well reservoir monitoring through ensemble Kalman filter. In: Paper Presented at SPE/DOE Improved Oil Recovery Symposium, SPE 75235. Society of Petroleum Engineers, Tulsa, OK, 13–17 April 2002.
- Oliver, D.S., Chen, Y., Nævdal, G., 2011. Updating Markov chain models using the ensemble kalman filter. *Comput. Geosci.* 15 (2), 325–344. <https://doi.org/10.1007/s10596-010-9220-4>.

- Park, Jaeyoung, Datta-Gupta, Akhil, Singh, Ajay, Sankaran, Sathish, 2021. Hybrid physics and data-driven modeling for unconventional field development and its application to US onshore basin. *J. Petrol. Sci. Eng.*, 109008 <https://doi.org/10.1016/j.petrol.2021.109008>. In press.
- Pascanu, R., Mikolov, T., Bengio, Y., 2013. On the difficulty of training recurrent neural networks. In: International Conference on International Conference on Machine Learning. PMLR, pp. 1310–1318. Atlanta, USA, 16–21 June 2013.
- Prélat, A., Hodgson, D., Flint, S., 2009. Evolution, architecture and hierarchy of distributary deep-water deposits: a high-resolution outcrop investigation of submarine lobe deposits from the Permian Karoo Basin, South Africa. *Sedimentology* 56, 2132–2154.
- Pyrcz, M.J., 2004. Integration of Geologic Information into Geostatistical Models. University of Alberta, Canada. PhD Thesis.
- Pyrcz, M.J., Deutsch, C.V., 2014. Geostatistical Reservoir Modeling, second ed. Oxford university press, New York.
- Pyrcz, M.J., Sech, R.P., Covault, J.A., Willis, B.J., Sylvester, Z., Sun, T., 2015. Stratigraphic rule-based reservoir modeling. *Bull. Can. Petrol. Geol.* 63 (4), 287–303. <https://doi.org/10.2113/gscpgbull.63.4.287>.
- Radford, A., Metz, L., Chintala, S., 2015. Unsupervised Representation Learning with Deep Convolutional Generative Adversarial Networks arXiv preprint arXiv: 1511.06434.
- Santos, J., Xu, D., Jo, H., Landry, C.J., Prodanović, M., Pyrcz, M.J., 2020. PoreFlow-Net: a 3D convolutional neural network to predict fluid flow through porous media. *Adv. Water Resour.* 138, 103539. <https://doi.org/10.1016/j.advwatres.2020.103539>.
- Santos, Javier E., Yin, Ying, Jo, Honggeun, Pan, Wen, Kang, Qinjun, Viswanathan, Hari S., Prodanović, Masa, Pyrcz, Michael J., Lubbers, Nicholas, 2021. Computationally Efficient Multiscale Neural Networks Applied to Fluid Flow in Complex 3D Porous Media. *Transport Porous Media*. <https://doi.org/10.1007/s11242-021-01617-y>. In press.
- Sarma, P., Durlofsky, L.J., Aziz, K., 2008. Kernel principal component analysis for efficient, differentiable parameterization of multipoint geostatistics. *Math. Geosci.* 40 (1), 3–32. <https://doi.org/10.1007/s11004-007-9131-7>.
- Srivastava, N., Hinton, G., Krizhevsky, A., Sutskever, I., Salakhutdinov, R., 2014. Dropout: a simple way to prevent neural networks from overfitting. *J. Mach. Learn. Res.* 15, 1929–1958. <https://doi.org/10.5555/2627435.2670313>.
- Straub, K.M., Pyles, D.R., 2012. Quantifying the hierarchical organization of compensation in submarine fans using surface statistics. *J. Sediment. Res.* 82 (11), 889–898. <https://doi.org/10.2110/jsr.2012.73>.
- Straub, K.M., Paola, C., Mohrig, D., Wolinsky, M.A., George, T., 2009. Compensational stacking of channelized sedimentary deposits. *J. Sediment. Res.* 79, 673–688. <https://doi.org/10.2110/jsr.2009.070>.
- Sullivan, M.D., Foreman, J.L., Jennetteet, D.C., Stern, D., Jensen, G.N., Goulding, F.J., 2004. An integrated approach to characterization and modeling of deep-water reservoirs, diana field, western gulf of Mexico. In: Grammer, G.M., Harris, P.M., Eberli, G.P. (Eds.), *Integration of Outcrop and Modern Analogs in Reservoir Modeling*: AAPG Memoir 80. AAPG, pp. 215–234. <https://doi.org/10.1306/M80924C11>.
- Tan, X., Tahmasebi, P., Caers, J., 2014. Comparing training-image based algorithms using an analysis of distance. *Math. Geosci.* 46 (2), 149–169.
- Vo, H.X., Durlofsky, L.J., 2016. Regularized kernel PCA for the efficient parameterization of complex geological models. *J. Comput. Phys.* 322, 859–881.
- Wang, Y., Straub, K.M., Hajek, E.A., 2011. Scale-dependent compensational stacking: an estimate of autogenic time scales in channelized sedimentary deposits. *Geology* 39 (9), 811–814.
- Xie, Y., Cullick, A.S., Deutsch, C.V., 2001. Surface-geometry and trend modeling for integration of stratigraphic data in reservoir models. In: Paper Presented at SPE Western Regional Meeting. Bakersfield, California, USA, 26–30 March 2001.
- Zhang, T., Tilke, P., Dupont, E., Zhu, L., Liang, L., Bailey, W., 2019. Generating geologically realistic 3D reservoir facies models using deep learning of sedimentary architecture with generative adversarial networks. *Petrol. Sci.* 16, 541–549. <https://doi.org/10.1007/s12182-019-0328-4>.